Distribution of Copper Electrochemical Nucleation Activities on Glassy Carbon: A New Perspective Based on Local Electrochemistry

Daniel Torres [a], Miguel Bernal [a], Annaëlle Demaude [a], Sajid Hussain [a], Laure Bar [b], Patricia Losada-Pérez [b], François Reniers [a], Jon Ustarroz [ac]*

[a] *ChemSIN – Chemistry of Surfaces, Interfaces and Nanomaterials, Université libre de Bruxelles (ULB), Campus de la Plaine, Boulevard du Triomphe 2, CP 255. 1050, Brussels, Belgium.*

[b] *EST – Experimental Soft Matter and Thermal Physics Group, Université Libré de Bruxelles (ULB), Campus de la Plaine, Boulevard du Triomphe, CP 223,1050, Brussels, Belgium*

[c] *SURF – Research Group Electrochemical and Surface Engineering, Vrije Universiteit Brussel, Pleinlaan 2, 1050 Brussels, Belgium*

* Corresponding Author: jon.ustarroz@ulb.be

ABSTRACT

The electrochemical nucleation and growth (EN&G) on active surface sites has been a concept of fundamental and technological interest for several decades. Here, we have studied the EN&G of Cu on glassy carbon with a new perspective using the Scanning Electrochemical Cell Microscopy (SECCM), in combination with scanning electron microscopy, atomic force microscopy, and X-ray photo-electron spectroscopy. Unlike the conventional macroscopic approach, we leveraged the spatial resolution of the SECCM to probe individual sites on the same surface, independently from each other, revealing regions with different energy barriers for nucleation and a distribution of activities for EN&G at the microscopic scale. This site-dependent activity can be modified with common surface pretreatments (i. e., polishing and preanodization). We addressed the electrochemical diversity through multiple descriptors and used them to conduct statistical analysis, supported by surface characterization techniques, bringing forward information that is simply unavailable with the conventional macroscopic approach. This work serves as a departure point to conceive new analysis strategies and address the real nature of active sites for nucleation.

INTRODUCTION

The electrochemical nucleation and growth (EN&G) of a new phase on a foreign substrate has been a concept of fundamental and technological interest for several decades. The early stages of the birth of a new phase correspond to the formation of small clusters of atoms (or atom aggregates) called nuclei, onto specific (active) sites on the surface, becoming building blocks of the two-dimensional or three-dimensional new phase [1,2]. EN&G is quite a complex process made up of many events that proceed simultaneously, including the adsorption of precursors on the electrode surface (adatoms), the surface diffusion of adatoms, the formation of nuclei, followed by their growth by direct attachment and/or their surface diffusion, and coalescence and aggregation [3,4], driven by the minimization of the imposed supersaturation.

In electrochemical nucleation, the supersaturation, *i. e.*, excess Gibbs free energy, can be externally imposed through the proper instrumentation by controlling the electrical potential of the system. This makes the EN&G process an effective and convenient method to functionalize a surface by the direct growth of nanostructures with diverse morphologies, cluster sizes, and distributions that can be tuned with the experimental parameters in view of the foreseen application. Rational design of the active surface structure is key to many energy conversion & storage schemes [5], including (photo)electrocatalysts, fuel cells, and battery technology [6–8].

Since electrodeposition offers a large experimental parameter space with a lot of opportunities for improvement, research is often based on empirical data, and the fundamental notions of EN&G, especially about the initial stages, remain poorly understood. The conceptual framework for the understanding of EN&G has been reviewed many times [1,2,9–12], with the foundation layout by the early work of Fleischmann and Thirsk [13]. The experimental approach to the kinetics of nucleation consists, typically, of deriving the dependence of the nucleation rate on supersaturation, which is directly proportional to the number of active sites on the surface [14,15]. A theoretical description of the study of multiple nucleation on active sites under diffusion control growth was made available by Scharifker and Hills [16], and later by Mostany [17,18]. Under the assumption that there is a limited number of energetically uniform active sites on the surface, instantaneously frozen with the overpotential applied, which decrease over time by the development of exclusion zones: the overlap of the diffusion fields around the irreversibly growing nuclei creates a concentration depletion, decreasing the probability of nucleation in its neighborhood. As these zones spread, they capture the latent nucleation sites stopping them from taking part in the process. Thus, the exclusion zones introduce correlation in the spatial distribution of nuclei [19–21].

Inevitably, the notion of an active site as the preferred site of the surface onto which the nucleation occurs with the highest probability accompanies all theoretical and experimental studies of EN&G on a foreign substrate. The number (and activity) of these sites define the nucleation (and further growth) process since the total number of nuclei formed cannot exceed the number of active sites on the surface [22]. Those can be rationalized as being steps, kinks, holes, grain boundaries, edges, defects, etc.; chemically or physically distinct locations on the surface which could promote nucleation.

The assumption of uniform activity, i. e., the active sites being independent of each other and having the same probability of activation, is a common yet controversial topic of discussion. Being a relevant concept in every heterogeneous process, little is known about what renders a site *active* for nucleation and their distribution on the surface. Moreover, there is no clear definition to

gauge the activity of a specific site for a given experimental condition, besides the notion that it is related to the specific rate of the reaction taking place. The work of Markov and Kaischew [23,24] introduced the notion that the number and activity of sites were potential-dependent, whilst Fletcher and Lwin [25] proposed that the activities are distributed in a spectrum, characteristic of the electrode surface. The latter brings forward the role of the surface state in determining how the nuclei are formed in the first place. Furthermore, the active sites can be understood as chemical reaction sites [26] which could appear or disappear during the nucleation process due to concomitant (electro)chemical surface transformation reactions [27]. In any case, the classical approach to describing microscopic events from macroscopic properties measured over the whole electrode area cannot account for differences that may arise at the microscopic level. Therefore, what is measured conventionally can only result in an averaged value that levels out the local differences in the nature of the surface sites involved in nucleation [27–29].

In the last decades, thanks to advances in instrumentation, several approaches have been developed to address the role of the surface state in the nucleation process through microscopy techniques [30–34]. This put in perspective the need for spatially resolved techniques to probe the diversity of active regions and provide information about the local distribution of activities on a given surface. Similarly, experiments using micro and nano- electrodes where single isolated sites are expected [35], have provided accurate information about critical nuclei formation and individual nucleation rates; it also becomes possible to resolve individual events during the electrochemical response, observed as discrete current spikes, which may have been caused by the formation of one nucleus [35–37]. Although this approach was able to provide very important aspects about EN&G, micro and nano- electrodes cannot easily address the distribution of active sites. In addition, the construction and control of an electrode of such dimensions can be a technical challenge, and not all materials are available. In this perspective, Scanning Electrochemical Cell Microscopy (SECCM) has emerged as an ideal probe-based technique to characterize the electrochemical interface and surface activity at the μm–nm scale [38–40], allowing the use of any substrate which could be conventionally used for any electrochemical experiment. The electrochemical measurements are performed within a confined region of the electrode surface, defined by the dimensions of the meniscus formed at the end of an electrolyte-filled pipette probe containing a quasi-reference counter electrode (QRCE). Since the studies of electrochemical nucleation are extremely sensitive to the state of the surface, extreme care is needed to obtain reproducible and meaningful results, which often come at the expense of time-consuming protocols to prepare the electrode surface. In this case, the SECCM provides the capability to probe single regions with isolated sites over the same macroscopic surface, making each experiment on a fresh region. This protocol can be repeated semi-automatically in a high-throughput fashion, giving access to a large array of independent measurements, which are used to build up spatially resolved maps of electrochemical features and topography, accordingly [41].

Among many other applications, this probe-based approach has been deployed to screen the intrinsic activity of isolated catalytic sites for a variety of reactions, including electrodeposition: the study of EN&G of silver on HOPG has been described as a non-continuous process at the nanoscale and revealed that the nucleation is not confined to the step edge sites, as was previously proposed [34,42], and in fact, can occur to a significant extent on basal plane sites [43]; Pd and Pt electrodeposition has been carried out on single-walled carbon nanotubes to study the factors controlling the physical features of the deposit [44], and in carbon-coated TEM grids to

highlight the possibility to correlate the electrochemical data with subsequent microscopy characterization, respectively [39,45]. However, these previous studies do not address the spatial distribution of active sites on the carbon-based substrates, nor the ability of the probe to isolate a comparatively smaller number of active sites.

Recently, our group has used this novel approach to explore the electrochemical nucleation, growth, and dissolution of Au nanoparticles in a glassy carbon (GC) substrate, showing the onset potential for nucleation to be site and size -dependent [46]. In this contribution, we use SECCM to probe the EN&G of copper in multiple regions of a glassy carbon surface, and we provide direct evidence and a thorough analysis of the diversity of the activity of this substrate towards nucleation and its variation with the surface state. Electrodeposition of copper has been one of the most studied systems in fundamental studies of EN&G, which makes it an ideal electrodeposition system to explore with a novel local approach that aims at offering a new perspective of the electrochemical nucleation and growth process. GC was selected as the substrate because it possesses diverse surface features that allow studying the distribution of the active sites in a wide potential window [47]. We employ a large dataset to provide a statistical analysis of the nucleation process. We further consider and discuss what renders a site *active* for nucleation based on typical electrode pretreatments used conventionally to explore metal electrodeposition, bringing forward information with this locally-resolved technique that is simply unavailable with the conventional macroscale approach.

EXPERIMENTAL

Chemicals and Electrodes materials

All reagents were of analytical grade and were used as received: Copper Sulfate ($CuSO_4$, anhydrous, 98%, Alfa Aesar) and Sulfuric Acid (H_2SO_4, 96%, Merck) were used to prepare a solution of 0.4mM $CuSO_4$ + 0.5M H_2SO_4 in deionized water (18.2 M Ohm at 25°C). Glassy carbon square substrates (Sigradur G Plates, HTW) were used after being washed in 5 min intervals in a sonic bath with deionized water, isopropanol, and deionized water, then dried under nitrogen gas flow. The as-received substrate with a mirror finishing was considered the *pristine* sample for these experiments (hereafter referred to as such). The *polished* substrate was produced through mechanical polishing of a pristine GC plate with a microcloth and alumina powder of 1 µm. The 1 µm size powder was chosen to introduce changes to the surface on the same scale as the electrochemical probe. For the *preanodization*, the substrate was subjected to 30 s polarization in an oxidative potential (0.2 V).

Macroscopic electrochemical setup

Macroscopic scale experiments were conducted in a three-electrode cell controlled with an Autolab potentiostat (Metrohm). Glassy carbon plates were used as working electrodes (WE), and Pt ring and Pt wire as counter and pseudo-reference electrodes, respectively. A Pt electrode was chosen as pseudo-reference for comparative purposes with the microelectrochemical setup. The solution was held in a meniscus configuration with the help of an inert O-ring (EPDM, 10 mm in diameter) and purged before each experiment. All potentials hereby are reported vs the Pt/H_2 system (see Section S1 in the supporting information). In this work, we use the term *macroscale* to refer to the electrochemical experiments conducted in a conventional setup in which the dimensions of the electrodes are in millimeters.

Microelectrochemical characterization: SECCM setup

Micro-electrochemical experiments were performed using a custom-built SECCM workstation. Single-barrel pipette probes (see Section S2 in SI) were back-filled with electrolyte solution, with a Pt wire quasi-reference counter electrode placed carefully inside and mounted on a holder with a Z-direction piezoelectric positioner (Nano-MET10, MadCityLabs). The GC substrates were placed on a motorized sample stage mounted on X-Y positioners (Nano-M250, MadCityLabs). The position of the pipette relative to the substrate was closely monitored with an optical camera. Custom-built potentiostat featuring current collectors with a sensitivity of 1nA/V, and a data collection system (PCIe-7856R FPGA card, National Instruments) were controlled by LabVIEW (2018, National Instruments) interface running the Warwick electrochemical scanning probe microscopy software (WEC-SPM, www.Warwick.ac.UK/electrochemistry). The sampling time was

40 µs and the number of samples per data point was 256. The setup was installed inside a home-build faraday cage equipped with acoustic insulation panels (Kevothermal) and aluminum heat sinks mounted on top of an optical table with automatic leveling isolators to reduce perturbations from sounds, mechanical vibrations, electrical noise, and/or thermal drift.

Electrochemical data were collected at multiple points using a hopping-mode protocol. In brief, the SECCM probe was approached to the WE surface in a series of predefined locations forming a rectangular grid (typically 60 x 60 µm). The contact of the probe with the substrate was established by monitoring the current of the substrate as the micro-electrochemical cell was formed with the QCRE. Upon each landing, an independent electrochemical measurement was made to acquire an independent and spatially-resolved electrochemical profile of the substrate (see Fig 1c). The final position of the X, Y, and Z-piezo positioners at each landing is used to construct the apparent topographical map of the WE probed area, as the distance of the landing in function of the lateral position (Z-coordinate). The separation between each landing spot was maintained relatively large (5 µm) to avoid any overlapping between contiguous measurements, we consider this approach as random sampling since the distance between each point is significantly large. Although the SECCM can provide topography information based on the Z-axis resolution, this is not the case for these experiments due to the relatively large size of the pipette's diameter chosen here. Therefore, we refer to the topography information inferred from the SECCM as *apparent topography*. The collected electrochemical information was processed to extract the relevant magnitudes, from which statistical analysis was conducted, using custom software developed on Igor Pro 6 (Wavemetrics) and Python. The onset potentials were estimated by two protocols: (i) by means of a non-linear polynomial fitting to the i/E experimental curves, the minimum of the first derivate corresponds to the potential E at which the current i start to rise predominantly. (ii) by selecting the value of E at which the current i reaches 5% of the peak current. The latter was systematically deployed for all the i/E; the former was used for comparative purposes. Visual inspections were performed on samples of the data to ensure the consistency of the estimations. This approach allowed us to extract systematic information of every cyclic voltammetry experiment with consistency, in order to construct each pixel of the spatially-resolved maps and build the dataset to conduct the statistical analysis.

Surface Characterization

Atomic force microscopy (AFM):
AFM measurements were performed using a JPK Nanowizard 4BIO-AFM from Bruker (Nano GmbH, Berlin, Germany). Measurements in air were carried out in tapping mode (named "AC-mode imaging") using PPP-NCL-W probes (Nanosensors, Neuchatel, Switzerland) with a cantilever length of ~225 µm, and a spring constant of ~48 N m^{-1}. The working resonance frequency was ~150 kHz. Images of 256 pixels were done at room temperature with a setpoint of 0.5V, a gain of 300, and a line rate of 1Hz. The images were analyzed and extracted using JPK Data Processing software, version 7.0.137.

Scanning electron microscopy (SEM):
The micrographs were acquired using a JEOL JSM-7100F Field Emission Scanning Electron Microscope, operating at 15 kV, with a working distance of 10 mm. The images were analyzed using ImageJ software.

X-ray photo-electron spectroscopy (XPS):
The XPS analysis was performed with a PHI - VersaProbe II spectrometer from Physical Electronics. Spectra were acquired with a monochromatic Al Kα X-ray source (52.98 W), 100 µm diameter analysis areas, and subsequently analyzed with CasaXPS© software. The peaks were deconvoluted with a Gaussian-Lorentzian peak and a Shirley background. The pass energy for the survey and high-resolution spectra were 93.9 and 23.5 eV, respectively.

RESULTS

A new microscopic perspective of electrodeposition

The electrochemical deposition of a new phase can be followed in situ by recording the current flowing through the electrode/electrolyte interface. Conventionally, cyclic voltammetry (CV) is used to characterize the interface, as it produces a spectrum of signals along with the potential window, serving to identify the regions at which the electrochemical activity can be observed.

Fig. 1a shows the resulting voltammogram recorded at 100 mV/s in Cu^{2+} electrolyte on a pristine GC electrode of 10 mm in diameter. The CV exhibits the familiar features associated with the electrodeposition and electrodissolution of metals on a low-energy surface: small currents close to zero during the initial part of the forward scan precede the onset potential (OP) of the current rise, due to the discharge of Cu^{2+} to Cu. The swift depletion of Cu^{2+} from the interface leads to a cathodic peak at -1.1 V and further current stagnation when reaching a diffusion-controlled regime. In the reverse scan, the current branches cross over each other, forming a current loop, typical of Volmer-Weber electrochemical nucleation and growth mechanism, where deposition of Cu onto preformed Cu islands is favored over Cu deposition on bare GC [14,48]. At more positive potentials, the dissolution of the deposit formed during the forward scan begins, with an anodic peak at -0.3V.

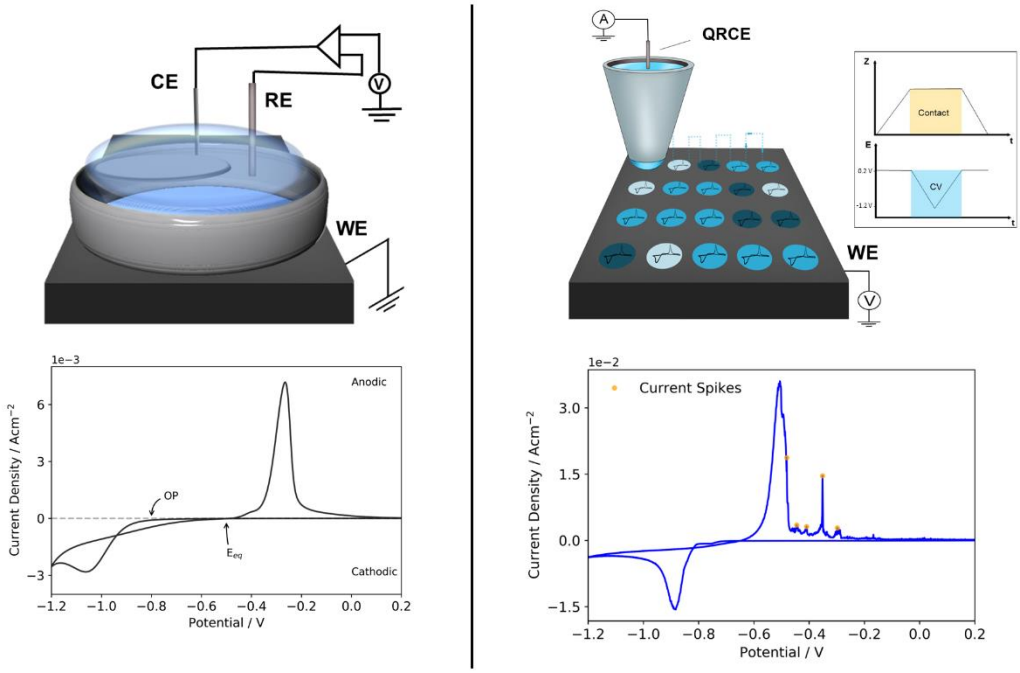

Fig 1. (a) Schematic of the macroscale characterization setup, using a glassy carbon plate as a WE, and (b) the representative voltammetric response of electrodeposition of copper at 100 mV/s. (c) Schematic overview of the microscale cell setup deploying the SECCM in hopping-mode. The blue circles indicate the probed regions of the working electrode and the arrows indicate the movement of the pipette probe. The inset shows the pipette-to-substrate separation (Z-axis) and the potential E profile over time. (d) Shows a typical voltammetric response for electrodeposition of copper recorded at 100 mV/s with the SECCM.

Although in many experimental works the CV is only analyzed qualitatively, it is possible to extract relevant electrochemical descriptors such as: (i) the onset potential, (ii) the equilibrium potential (E_{eq}), and (iii) the ratio between the charge transferred during the anodic dissolution scan and cathodic deposition scan (Q_a/Q_c). For the study of EN&G, it is relevant to consider the onset potential (OP) of the CV experiment, as the point at which the cathodic current starts to rise (Fig 1b). Given that nucleation is an activated process involving an energy barrier [2], the OP serves as an appropriate descriptor, marking the potential at which the energy barrier for nucleation is overcome [49]. For this systematic approach, the OPs were defined by selecting the value of potential E at which the cathodic current reaches 5% of the cathodic peak current. The difference between the OP and the E_{eq} defines the overpotential needed for nucleation. The charge ratio Q_a/Q_c and the difference of the onsets of consecutive scans are also useful descriptors to assess the nature of the surface state since this can be compromised by leftovers from the first scan: often the anodic dissolution is incomplete, which frequently eases the nucleation in subsequent

scans shifting the OP to more positive values (lower overpotential). The charge ratio describes the efficiency at which the charge consumed during the electrodeposition is accounted for during the dissolution process, a ratio of 1 would indicate that the same amount of charge was transferred during both processes.

As in any heterogeneous process, the electrochemical nucleation is highly dependent on the condition of the electrode surface. When we perform the CV in the conventional macroscopic electrochemical cell, the whole surface is involved in the process. In this way, it is only possible to obtain one single response that reflects the convolution of the contributions of millions of active sites. This single response cannot possibly account for all the differences that might arise at the microscopic scale. To overcome this limitation, we employed the probe-based approach of the SECCM to characterize the electrodeposition of copper at the local level. As schematized in Fig 1c, the SECCM local electrochemical measurements are performed at the confined region of the surface defined by the meniscus at the end of the probe. The microscopic electrochemical cell that is created allows us to evaluate the same EN&G process as the macroscopic approach, but on independent regions of the same surface. In this way, not only the electrochemical deposition process is evaluated in a very small region of the substrate; but also any possible interaction between neighboring regions is eliminated, which, as will be discussed later in the manuscript, has important implications for the nucleation and growth process: the activity of a region can be evaluated without being affected by possible concentration depletion regions initiated in adjacent regions. The WE area of the local cell has been estimated from the meniscus “footprint” visualized with SEM (diameter ~ 3 µm, see Fig S3 in section S2 of SI), enabling the normalization of the CVs.

Fig 1d shows a characteristic voltammogram recorded at 100 mV/s on the pristine GC electrode with the SECCM. At first inspection, the local CV exhibits the same overall profile as the macroscopic measurement (Fig 1a), namely, the display of a cathodic peak and a characteristic current loop. These features are consistent with a three-dimensional EN&G process on a foreign substrate. However, contrasting differences are also found between the two approaches: whilst in the macroscopic cell, the anodic peak is rather sharp and symmetrical, with no electrochemical activity going further, in the microscopic cell, an unexpected diversity of current spikes can be seen along with the anodic scan, just after reaching the anodic peak. It must be noted that similar features have also been obtained in similar electrodeposition/electrodissolution experiments from a 1 mM $HAuCl_4$ solution [46]. Such discrete current spikes have been associated with individual dissolution events, which can be resolved when monitored at the microscopic scale. Current spikes can also be observed during the evaluation of the electrochemical response on nanoelectrodes [35–37].

The voltammetric response was also explored at different scan rates. The voltammograms in Fig S4a and S4b, section S3 of SI were recorded at 10 mV/s and 1000 mV/s, respectively. A particular observation in these experiments is the influence of the scan rate on the number and shape of these anodic spikes: at 10 mV/s the anodic current spikes are large and persistent, whereas at 1000 mV/s the anodic wave exhibits a conventional symmetrical peak, and no current spikes were significantly detected. This difference is related to the fact that slow scan rates spend longer times in each potential step, giving more opportunities to resolve individual events. Time and potential-dependent surface transformation processes are subjects of active research in our lab but fall out of the scope of this particular manuscript.

These results show qualitatively the diversity of the electrodeposition process when this is monitored at the microscale and the impact of confining the electrochemical interface. To analyze such diversity, we performed hundreds of individual measurements on pristine and modified GC surfaces and extracted from them relevant electrochemical descriptors to gain a new spatial and statistical perspective of the electrodeposition process.

Spatially resolved electrochemical data

For the first experiments, we employed a fresh GC substrate without further modification. The SECCM was deployed in a "hopping-mode" to perform high-speed, spatially-resolved local experiments, as schematized in Fig 1b. In hopping-mode protocol, the SECCM probe is scanning across the GC surface stepwise, establishing a local electrochemical cell and launching an independent CV with each landing. The landing positions in our hopping CV are exaggeratedly far from each other since it is utterly important that each new position is fresh and has not been altered by a previous measurement, this was later corroborated by SEM images (Fig S3 in Section S2 of SI). By extracting relevant magnitudes from the CVs a map of the electrochemical descriptors of interest can be traced.

Fig 2 shows a collection of spatially resolved electrochemical data (i. e., maps) extracted from a set of individual CVs performed on hopping-mode by scanning the GC surface in a (rectangular) grid. By representing the variation of the electrochemical data with a color scale, we can easily visualize the spatial distribution of the features on an 80 x 80 µm region of the surface.

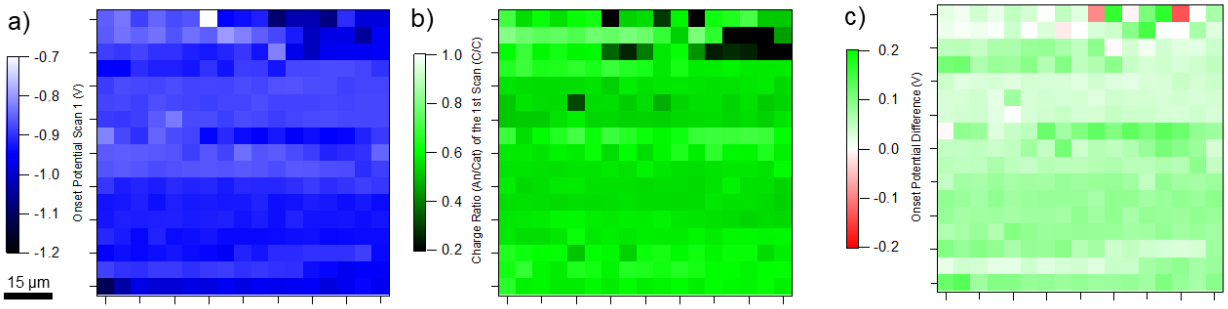

Fig 2. SECCM mappings of a) the onset potential of the first scan, b) the charge ration Q_a/Q_c and c) the OP difference between the first and second scan on an 80 x 80 µm region of the pristine GC. Each data point from the maps is separated by 5µm. A scale bar is included for reference.

At first glance, the map of the OP (Fig 2a) reveals a spatial diversity of the electrochemical activity in a relatively small region (80 x 80 µm), highlighting the extreme sensitivity of the nucleation process to the local state of the surface (maximum and minimum onset potentials for Cu nucleation of -1.09 V and -0.799, respectively). We can encounter regions with differences of

hundreds of mV in onset potential within a few micrometers of each other. The ohmic drop can be considered neglectable in the SECCM configuration given the small faradaic currents that are measured, then, the source of the overpotential and such diversity could be related to the difference in activity (and/or number of active sites) among the microscopic regions probed [50] or to the stochastic nature of the nucleation process itself, which becomes especially relevant in the spatially-confined regime [51]. When the probe area is small enough the probability of finding an active sites decreases, this phenomenon can manifest itself as induction times, i. e. period of time after the overpotential is applied in which no nuclei are formed [35,36,52], or, in this case, as shifts in the OP to more negative potentials. This site and size- dependent response can only be revealed when having access to the microscopic scale.

Moreover, the spatial diversity of the charge ratio Q_a/Q_c (Fig 2b) and the difference between OPs of consecutive scans (Fig 2c) is also remarkable. Visually, it is clear that the charge consumed during the electrodeposition can hardly be accounted for during the anodic dissolution process in this potential window since the ratio Q_a/Q_c is far from 1 in all sites. The OPs difference map (Fig 2c) also shows a spatial diversity consistent with the OP map (Fig 2a), with most of the cases shifting towards the positive direction (OP of 2nd scan more positive than OP of 1st scan). This is expected: a consecutive scan exhibiting a more positive OP (lower overpotential) means that the electrodeposition requires less energy to proceed in this instance. This is usually due to Cu leftovers that remained on the surface (incomplete anodic dissolution) which can act as the new growth centers; or to the transformation of the surface state once it has been subjected to prolonged polarization, resulting in an activated surface. This is consistent with the observation of ratios $Q_a/Q_c < 1$ (Fig 2b), suggesting that the anodic dissolution was indeed incomplete during the CVs. Although the droplet configuration can promote a rapid oxygen saturation in the cell, we do not consider it to be an important factor for the charge ratio due to the (lack of) catalytic activity of GC and Cu itself towards oxygen reduction [53]. Yet, we must recognize the possibility of particles detaching from the surface to account for the low charge ratio [43]. Unexpectedly, we can also find shifts to the negative direction (red points in Fig 2c map), i. e., when the 2nd onset potential is more negative than the 1st. It is not clear what can cause such behavior, but an argument can be made to consider a transformation of the surface which renders it less active, forcing a shift to more negative potentials. These considerations fall beyond the scope of this manuscript but are discussed in other work from our group [46].

Interestingly, an overall look at the different maps reveals a spatial correlation among them. For example, a more positive OP (light blue points in Fig 2a) corresponds with a lower charge ratio in Fig 2b, which is subsequently correlated with a small OPs difference (light green points in Fig 2c). This is likely due to the fact that a more positive OP means a longer time in the cathodic region of the CV, leading to a larger cathodic charge, $Q_c >> Q_a$. In turn, this did not translate to a larger OPs difference, meaning that there might be dissolution mechanisms that are not being accounted for during the anodic scan (e.g., nanoparticles detachment), or that the activity of such site was already high, that would not shift even if some leftover did remain. The statistical significance of these results will be further discussed in the subsequent section.

A statistical representation of the electrodeposition process

The site-dependent electrochemical activity that can be revealed at the microscopic scale is, of course, averaged out when looking at it from the macroscopic perspective (Fig 1a), given the convoluted nature of the single electrochemical response obtained in such condition. However,

the diversity encountered plays a titular role during the initial stages of the electrodeposition process. Therefore, it is essential to reveal it and understand its origin and impact on the properties of the nanostructures that are being deposited. To shed more light on the diversity of the electrodeposition process, we collected several data sets across the GC pristine surface and extracted the relevant electrochemical descriptors to perform statistical analyses.

Fig 3 shows the OP distribution for 3 different scan rates: 10 mV/s, 100 mV/s, and 1000 mV/s. The histograms were constructed with an average of 326 data points, each collected from an individual CV on a fresh spot on the surface, and the height has been normalized by the number of counts.

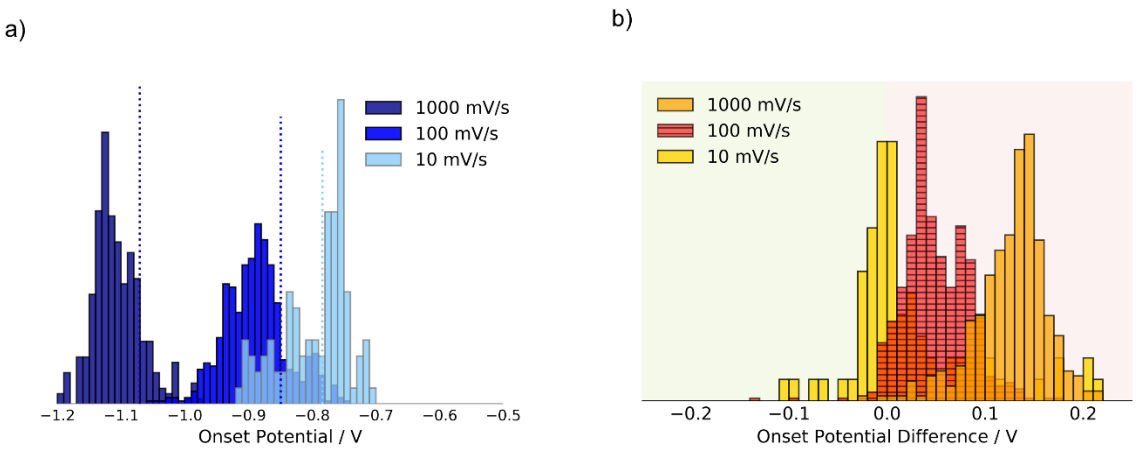

Fig 3. Histogram representation of the distributions of the OP of the first scan (a) and the OP difference between the first and second scan (b) at different scan rates. The dashed lines represent the corresponding value measured in the macroscale.

The OP histograms in Fig 3a confirm the intuitive observation from the mapping representation of Fig 2a: there exists a non-uniform distribution of electrochemical nucleation activities on the GC surface. The distribution spreads along a wide potential window with the most likely values clustering around the average, different for each scan rate. The average OP for 100 mV/s lies at -0.888 V with a standard deviation σ = 0.049 V. The average OP is more negative than the onset potential for the macroscale experiment, at -0.845 V. In fact, this is also the case for the other scan rates evaluated in the present study: with an average OP of -0.794 (σ =0.052) V and -1.109 (σ = 0.039) V at the microscale, -0.784 V and -1.071 V at the macroscale, for 10 mV/s and 1000 mV/s, respectively. These results can be attributed to the fact that the SECCM probes very small regions that are isolated from others. This allows us to take into account the contribution of each microscale region independently. At the macroscale, these contributions to the overall response are then rendered differently due to the convoluted nature of the process [19,54]: nucleation initiates in the most active regions so their contribution would be more important at the macroscale, leading to a more positive OP.

In general, a dependence of the OP with the scan rate is expected since an induction time is necessary before the nucleation and growth processes can proceed [55] (this is further confirmed by the trend in Fig S4d in SI). A longer induction time can manifest as a more negative OP in the potentiodynamic experiment. Our results show that the dispersion of the distributions in Fig 3a

slightly changes in terms of the standard deviation: 0.052, 0.049, and 0.039 V for 10, 100, and 1000 mV/s, respectively. If the dispersion were solely related to the induction time and stochastic nature of the nucleation, then a slow scan rate would lead to a narrow dispersion. However, our results show this not to be the case, therefore we can ascertain that the dispersion in the OP is mainly due to the heterogeneity of the GC surface: some microscale regions have more active sites for nucleation than others.

If we focus on the distribution at 100 mV/s in Fig 3a, we see that only 17% of the points exhibited a more positive OP (lower overpotential) compared to the macroscale. This is the percentage of sites that required less energy to overcome the energy barrier for nucleation. For 1000 mV/s and 10 mV/s, 14% and 56% of points have a more positive OP than this of the macroscale, respectively. By diminishing the scan rate, the time of residency at each potential step increases, this seems to lead to a superior activity or a higher number of active sites within the same region (i e., microscale OP of these regions is more positive than OP of the macroscale).

As seen in Fig 3b, the average OP difference between two consecutive scans becomes more positive at higher scan rates: 0.026V, 0.049 V, and 0.125 V, for 10 mV/s, 100 mV/s, and 1000 mV/s, respectively. A positive OP difference is indeed consistent and conventionally expected, given how Cu leftovers can enhance the nucleation in successive experiments. Nevertheless, OP differences of 0 V or even on the negative side can be found in the histograms. These unusual observations represent 41.6%, 6.3 %, and 0.6% of the total points for the populations obtained at 10 mV/s, 100 mV/s, and 1000 mV/s, respectively. Selected examples of unusual OP differences can be seen in Fig S5, section S3 of SI. The significant proportion of points with a lack of shift towards more positive OP can be considered as evidence of different dissolution mechanisms, that can also be related to the anodic current spikes (see Fig S4 in SI). The low scan rate promotes the formation of larger clusters than can detach but also subjects the surface to longer polarization time which could induce other reactions and/or surface transformations within the region, rendering the surface more inactive during the second scan.

The results presented so far serve to disclose the electrodeposition as a potential, time and site-dependent process, with great diversity at the microscale. This diversity manifests in several descriptors that can be extracted locally. Since the SECCM provides the means to access a large array of systematic experiments in a high-throughput fashion, it opens up the opportunity to look for correlations among the large pool of electrochemical data. To showcase this, we took a dataset recorded at 100 mV/s containing 289 individual measurements (represented as maps in Fig 2) and constructed a correlation matrix in which each square represents the correlation coefficient between two given variables. To compute the correlation, we opted for Spearman's coefficient (r_S), which assesses monotonic relationships (whether linear or not), since our data should not necessarily be linearly correlated to each other. As shown in Fig 4, the diagonal of the table is always a set of ones because the correlation between a variable and itself is always 1.

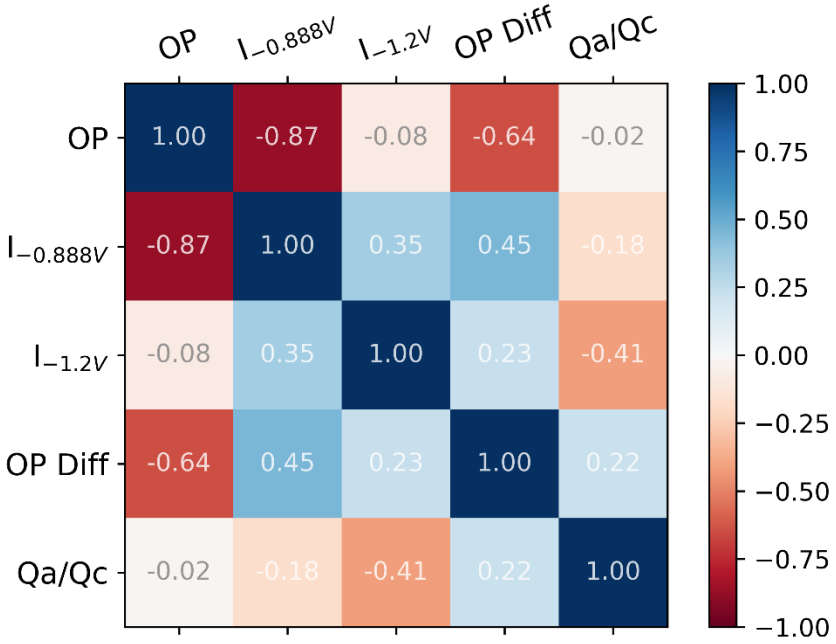

Fig 4. Correlation matrix (Spearman's coefficient) showing the relationship between the electrochemical descriptors at 100 mV/s at the microscale: Onset Potential (OP), OP difference (OP Diff), cathodic and anodic charge ratio (Q_a/Q_c), and the currents sampled at -0.888V ($I_{-0.888V}$) and $I_{-1.2V}$)

It can be verified that the OP is strongly correlated with the OP difference (r_S = -0.64). This correlation implies that the more positive the OP (surface more active), the less positive the OP difference, as if the region that is already highly active in the first place does not enhance its activity after the first scan. Yet, what renders the region highly active remains unclear. A similar correlation has been found for the electrodeposition of Au in GC [46]. Logically, there is a very strong correlation (r_S = -0.87) between the OP and the values of current at -0.888V (the average OP) collected on every CV. This correlation highlights how the current depends on the energy barrier for *nucleation*, given that the process is the formation of copper clusters on the GC fresh region. In contrast, when we evaluate the current values at -1.2 V, we see no correlation whatsoever (r_S = -0.08), signaling that the reaction is under a different regime (diffusion control), and the process of subsequent *growth* is independent of the initial energy barrier for nucleation.

The analysis of the dispersion of the electrochemical response as a function of the potential can be proven useful to establish the separation between two different regimes in a dynamic process. To study how the diversity at the microscopic scale contributes to the macroscopic response, Fig 5 shows the resulting voltammogram from the normalized sum of the individual measurements from the dataset recorded at 100 mV/s. The current values were sampled from the first scan of each microscale CV, for every potential value, then normalized by the number of data points. The reconstructed profile that we observe in Fig 5a is fairly similar to the one obtained with the macroscopic approach (Fig 1b), exhibiting consistent features with an EN&G process on a foreign substrate. Notably, the current spikes typically seen during the reverse anodic scan at the

microscale (Fig 1d) are not present, similar analysis showed the same effect for the electrodeposition/dissolution of Au [46]. These are random events that are leveled out when averaging the response, as it happens in the macroscale experiments themselves. The potential-dependent diversity of the electrochemical process is assessed in Fig 5b, 5c & 5d with a collection of box-and-whisker plots, describing the dataset of current values collected from each CV at specific potential steps. A box-and-whisker plot displays a five parts summary of a dataset: The minimum and maximum are represented in the whisker, and the first quartile, second quartile (i. e., median) as the red line in this case, and third quartile in the box itself.

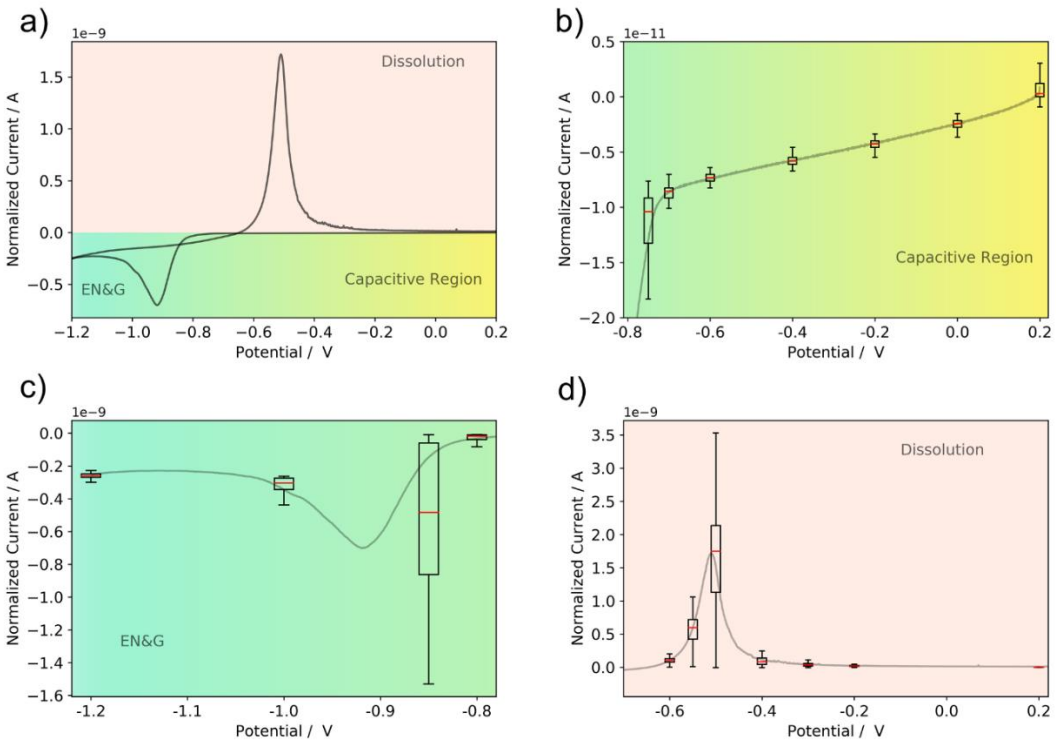

Fig 5. a) Voltammogram constructed from the normalized sum of individual local measurements recorded at 100 mV/s. The current values were sampled from the first scan of each microscale CV, the distribution of these populations is highlighted as box-and-whisker plots on different potential steps of the CV in b, c, and d.

For example, in Fig 5b, we see the evolution during the first part of the forward scan: at 0.2 V there is a relatively higher dispersion of values (represented as the wider box) which is expected, given that upon each landing, the formation of the double-layer and capacitive charging takes place and also pseudo-capacitive contributions due to oxidation/reduction of quinone-like groups common on carbon-based surfaces [56,57], which differs from site to site. The subsequent steps from 0 V to -0.5 V remain consistently tighter (low dispersion), given the absence of a reaction in the capacitive region. Once the faradic current starts to flow due to nucleation and growth, the dispersion of the current increases: At -0.75 V there is a decisively cathodic current flowing, and the greater dispersion in the box-and-whisker plot discloses it. With this representation, we can

clearly see a different behavior before and after -0.75 V, which marks the onset of a new process. As seen in Fig 5c, the dispersion is greatest at -0.888V where the reaction is driven by the formation of nuclei on active sites, independently from each other, and the box-and-whisker is skewed towards the negative side, meaning that a large portion of the current values is already discernible cathodic. After the cathodic peak, the current stagnates as the diffusion-controlled regime sets in; the dataset at -1 V becomes less dispersed, and finally, at -1.2 V the box plot is roughly symmetrical, showing that a new regime has been established. Whilst the former current values sampled at -0.888 V were greatly dispersed as the nucleation proceeded differently on each site, the latter at -1.2 V become independent of the potential as they converge under diffusion-controlled growth, set by the extension of the diffusion fields, which have overlapped within the meniscus and therefore defined by the meniscus and pipette geometries, similar on each site.

Analogously, the same analysis can be done for the anodic dissolution during the reverse scan in Fig 5d: The dispersion of the current values at -0.6 V marks the onset of the new process and is greatest around the anodic peak at -0.5 V. Whilst the surface is being depleted from the metal clusters, the current diminishes and so does the dispersion. A slightly positively skewed dataset at -0.4 V is probably due to the influence of the current spikes present in the microscale characterization.

Micro-Electrochemical characterization: The Effect of Surface Pretreatment

When the EN&G process is monitored at the microscopic scale, the differences among the active regions of the GC surface become apparent. The introduction of a distribution of activities for EN&G presented here opens up the questions of how (or if) this activity correlates with the local surface state; physical or chemical features that can be modified with the different pretreatment protocols for the electrode surface. To assess the effect of the surface state, we consider two customary pretreatments: mechanically polishing of the surface and prolonged polarization at an oxidative potential, i.e., preanodization. Both are common practices to secure reproducible and meaningful results in the study of EN&G [2].

In our case, the polishing can introduce changes to the surface on the same scale as it is being probed. To reveal those changes, the surface was characterized by AFM before and after the pretreatment. For the micro-electrochemical characterization, we followed the same protocol as the experiments in the previous section: a grid of individual CVs was recorded at 100 mV/s on the polished surface, the results are presented in Fig 6. The AFM image in Fig 6a shows the rather smooth initial condition of the GC surface, compared to Fig 6b where the typical pattern of scratches left by the mechanical polishing can be seen. This means that polishing is actually roughening the surface of the GC at the microscopic level. Visually, the mapping of the OP on each surface (Fig 6c & 6d) revealed the differences: the dispersion of the response on the pristine surface is greater, whilst on the polished (roughened) surface we found a more energetically uniform response overall, with less negative OP values on average (note that the same color scale has been used in both figures). This is confirmed by the histograms in Fig 6e & 6f: we see how the distribution of the OP on the polished surface has become narrower and is displaced to less negative potentials (lower overpotential), with an average OP of -0.559V (σ = 0.012 V), a

difference 0.329 V in the average energy barrier for nucleation respect to the initial (pristine) condition. These results show that not only is the distribution less dispersed, with 80% of the cases falling within a standard deviation from the mean, but also that the majority of the probed regions are more active for nucleation: the probability of finding regions with a low overpotential is higher on the polished surface. Considering the scales of the morphology (AFM) and the SECCM map, this indicates that, after polishing, the probability of finding more active sites within individual regions of ~ 3µm in diameter is increased. This implies that, although polishing may render a surface morphologically more heterogeneous (compare Fig 6a&b), it renders the same surface more electrochemically uniform at the microscale (compare Fig 6e&f). In other words, a heterogenous morphology does not necessarily translate directly into a heterogeneous EN&G response, but may translate into the opposite as well.

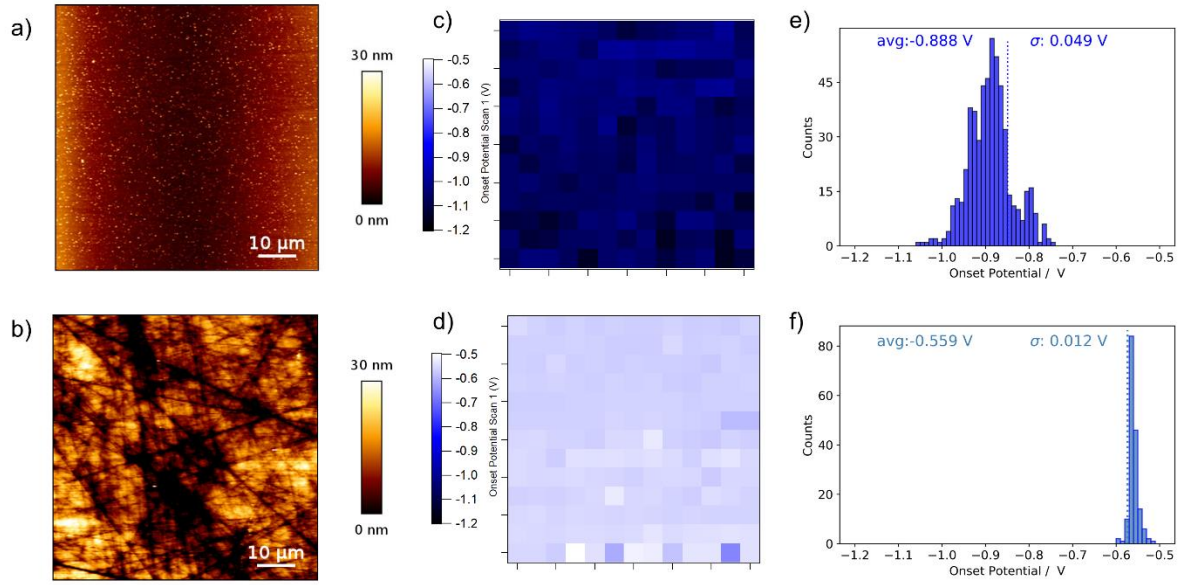

Fig. 6. AFM images of the GC surface before (a) and after polishing (b). Comparison of the spatial distribution of OP recorded on the pristine (c & e) and polished (d & f) GC surface. The dashed lines in e & f represent the corresponding value measured in the macroscale. The electrochemical characterization was done on a region of similar size as the AFM characterization, 60 x 60 µm.

Polishing is a typical pretreatment of an electrode surface made to eliminate any kind of impurities that might be adsorbed or to level-out a substrate. It is often considered that, for carbon-based electrodes, the pretreatment can activate the surface [58,59]. The apparent activation in this sense could be related to the physical changes induced to the GC surface and/or concomitant changes in surface chemistry (i.e., surface oxidation). These modifications of the physical/chemical features of the surface seem to exert a considerable influence on the distribution of electrochemical activity at the local level. Should the new surface defects act as the active sites for nucleation, then the introduction of a significant number of such defects through polishing would lead to a high number of regions being more active for nucleation. The existence of the defects on every probed region guaranteed a low overpotential, as the nuclei formed first onto these defects rather than on any other point within the same micrometric region, creating an

energetically-uniform response. It is also worth noting that such activation is also apparent in the macroscale since the OP value for the polished macroscopic electrode was -0.574 V, 0.275 V more positive than the initial condition.

We then considered the notion of changing the local surface state through preanodization. To avoid introducing any perturbations, the experiments were performed on a fresh pristine surface as follows: the local experiments were launched as described before, but once the meniscus made contact with the surface, instead of launching the CV experiment immediately, this was preceded by a 30 s standby time at an oxidative potential (0.2 V). This protocol ensures that the preanodization was local and during the same time for each experiment. Note that in electrodeposition voltametric studies, it is common practice to employ the initial CV potential, 0.2 V in our case, as the pretreatment potential. Besides, in Fig 5b we present the collection of box-and-whisker plots which discloses a bigger dispersion at 0.2 V than at lower potentials, suggesting that a longer residency time at 0.2 V could serve to modify the electrochemical response of the subsequent CV scans.

From this dataset, we can extract more electrochemical descriptors for the preanodization: the magnitude of the "current jumps" (I_{jump}), registered 0.1 s after applying the pretreatment potential E= 0.2 V, and the total charge passed during this pretreatment (Q_{pt}). These current "jumps" are due to the formation of the double-layer and capacitive charging during the formation of the electrode|meniscus interface and also pseudo-capacitive contributions due to oxidation/reduction of quinone-like groups common on carbon-based surfaces [56,57], which can be different from site to site. Fig 7a shows the apparent topography (Z Coordinate) and the mappings of I_{jump} (Fig 7b) and the OP of the subsequent CVs (Fig 7c). As a reference, Fig 7d includes a representative chronoamperogram to help visualize the typical profile of the current jump during the preanodization. Interestingly, the maps of Z Coordinate, I_{jump} and OP, reveal a spatial correlation among these descriptors: a higher current jump (magenta in Fig 7b) seems to lead to a less negative onset potential (light blue in Fig 7c) in the subsequent CV. Accordingly, these seem to be correlated to a topographical feature (black in Fig 7a) on the same region of the pristine GC surface. A lower Z coordinate means a higher surface feature, which could represent a morphological defect on the GC surface (equivalent to a grain boundary in a polycrystal). Fig 7e includes a histogram of the OP distribution highlighting, in lighter blue, the values in the central region.

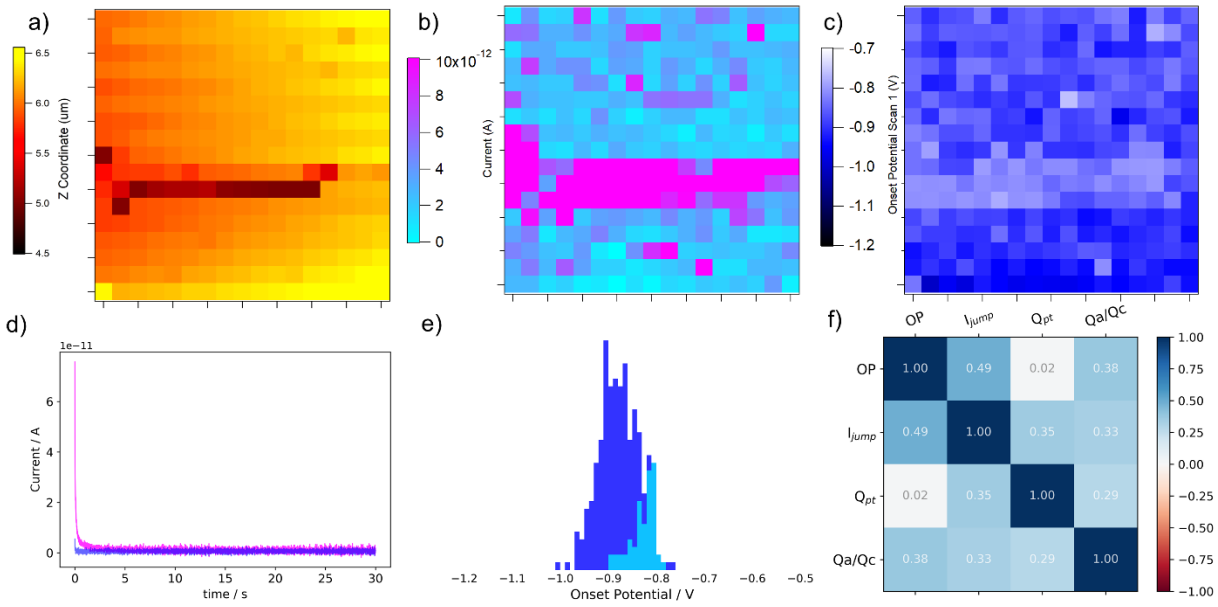

Fig 7. SECCM mappings of a) the apparent topography, b) the magnitude of the current "jump at t=0.1 s after applying the pretreatment potential E= 0.2 V and c) the onset potential of the subsequent CV. d) Typical current transient from two different regions (high and low current jump) of the map depicted in b. e) histogram of the OP distribution highlighting the values from the central region (lighter blue) of the map in c. f) Corresponding correlation matrix (Spearman's coefficient) showing the relationship between the electrochemical descriptors.

It is commonly considered that the preanodization can lead to increased activity of the electrode [32,47,57,60] (in fact, such pretreatment is often described as electrode activation), as well as to a more uniform response through the surface. With our results in Fig 7, we can attest that the preanodization instead of alleviating the local differences, effectively exaggerates them, resulting in a diversified response among the different regions. The scatter plot in Fig S7 (section S5 in SI) serves as an alternative representation of the same dataset, showing how the higher I_{jump} cluster around the less negative onset potential values, confirming the notion of activation on those regions. A first explanation for these results points to an electrochemical activation of specific sites on the central region of the map after being subjected to the prolonged anodic polarization, likely creating surface oxides which then acted as new active sites for nucleation. Yet, an alternative hypothesis that cannot be completely neglected is that the current jumps are higher due to those specific regions being more electrochemically active in the first place. However, we performed the same type of analysis in different microscopic regions of the GC surface and the correlation between I_{jump} and OP remains, but unrelated to topographical features (see Fig S8, section S5 in SI). This led us to believe that the first hypothesis is more plausible than the second one. To better visualize the correlations among the many descriptors, Fig 7f presents a correlation matrix constructed from the 289 measurements used to construct the maps.

With the Spearman's correlation coefficient, the moderate positive correlation between I_{jump} and the OP can be confirmed (r_S = 0.49). The positive sign indicates that the higher the current jump, the more positive the OP becomes, confirming the visual notions from the maps. Another

surprising result is the lack of correlation between the OP and the charge Q_{pt}, which would suggest that most of the charge involved in the oxidation of the region was consumed during the first instants (~ 0.1 s), and the subsequent standby time had no major influence whatsoever. As it is evident from the chronoamperogram in Fig 7d, the current quickly falls close to zero and stagnates after the initial jump. Monitoring the correlation of these descriptors can help us design better protocols to enhance the performance of the electrode towards metal electrodeposition: in this case, just 0.1 s of anodic polarization were enough to activate the substrate.

The comparison of the distributions of onset potential, as a descriptor of the energy barrier for nucleation, is useful to reveal the influence of the surface state on the electrochemical activity. In Fig 8, we have presented the distributions of OP from four different conditions: pristine GC surface (initial condition), after it has been polished, and under the effect of preanodization for both pristine and polished surfaces. The effect of polishing the surface is the most striking, displacing the average OP 0.32 V less negative, and narrowing the distribution further. The preanodization can also displace the average OP 0.041V less negative but tends to spread the distribution, evidenced by σ = 0.056 V, compared to σ = 0.049 V of the initial condition. The combination of both modifications can be seen in the polished + preanodization distribution, the average OP is displaced 0.027 V more positive, whilst the distribution becomes twice as dispersed (σ = 0.023 V), compared to the sample that was only polished.

Whilst the activation of the surface by polishing could be expected, the greater dispersion of the distribution of activities is a surprising result coming from the electrochemical pretreatment. The higher dispersion (differences among the regions are exaggerated) produces a wider range of possible activities on each region. The prolonged polarization could induce potential and time-dependent transformations of the surface, changing each region in an unexpected way. In contrast, polishing translates to a more active and energetically-uniform surface overall, enhancing the probability of finding a low barrier for nucleation. For clarity, the summary of all these electrochemical descriptors can be found in table 1. Interestingly, the macroscale OP only becomes 0.012 V more positive after preanodization. This means that, overall, the regions whose activity is exacerbated by preanodization (central part of Fig 7c) do not contribute enough to the macroscale response.

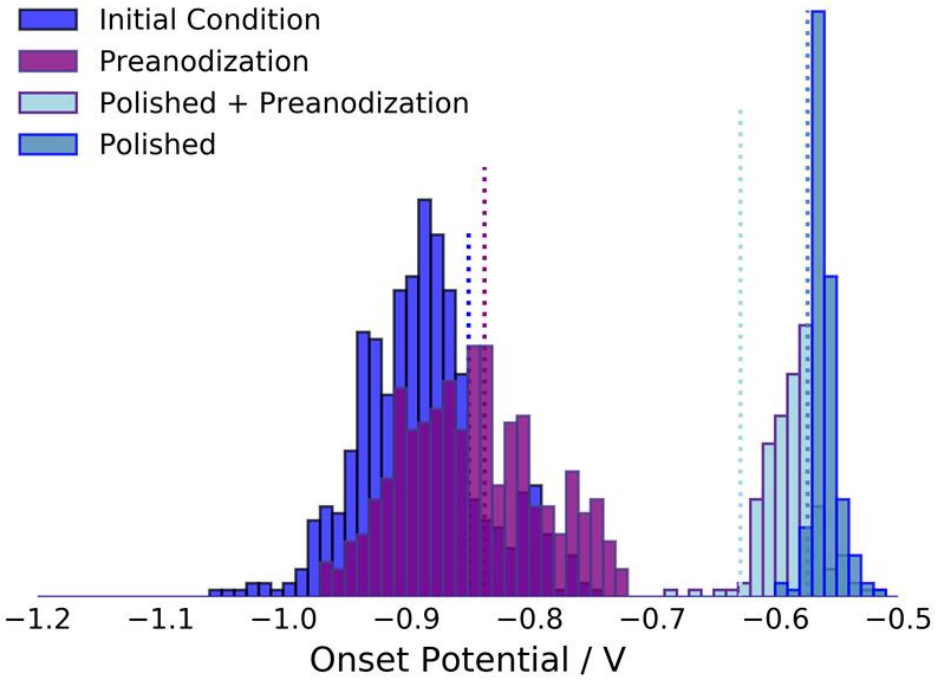

Fig 8. Distribution of the OP on the glassy carbon surface under different conditions: initial condition (average OP: -0.888 V), preanodization (-0.847 V), polished (-0.559 V), and polished + preanodization (-0.587 V). The height has been normalized by the number of counts. The dashed lines indicate the OP as measured in the macroscale.

Table 1. Summary of electrochemical descriptors for the different conditions

Condition	Average OP (microscale)	OP (macroscale)	Standard Deviation σ (microscale)	Average OP Diff (σ)	Average Charge Ratio (σ)	Distribution
Pristine (100 mV/s)	-0.888 V	-0.849 V	0.049 V	0.049 (0.033) V	0.57 (0.10)	
Pristine (**10 mV/s**)	-0.794 V	-0.784 V	0.052 V	0.026 (0.065) V	0.39 (0.03)	
Pristine (**1000 mV/s**)	-1.109 V	-1.071 V	0.039 V	0.125 (0.038) V	0.67 (0.04)	
Polished (100 mV/s)	-0.559 V	-0.574 V	0.012 V	-	0.35 (0.01)	
Preanodization (100 mV/s)	-0.847 V	-0.837 V	0.056 V	-	0.60 (0.11)	
Polished + Preanodization (100 mV/s)	-0.587 V	-0.638 V	0.023 V	-	0.37 (0.02)	

The Effect of Surface Pretreatment: Physical characterization

Our results so far have shown how diverse the electrochemical activity can be when it is monitored at the microscopic scale. To evaluate the effect of such diversity on the physical features of the deposit, we characterized the nanostructures electrodeposited on the different surface conditions by SEM. The Cu nanostructures were synthesized potentiostatically, at -1.2 V for 60 s, in the macroscopic cell as shown in Fig 1a. The electrodeposition conditions were chosen to overcome the kinetics limitations related to Cu two-stages reduction and to allow the metal clusters to grow for a sufficiently long time to attain sizes that enabled the observation of large populations. For the preanodization, an additional potential step of 30 s at 0.2 V was applied before the negative potential step. The resulting images and histograms are shown in Fig 9.

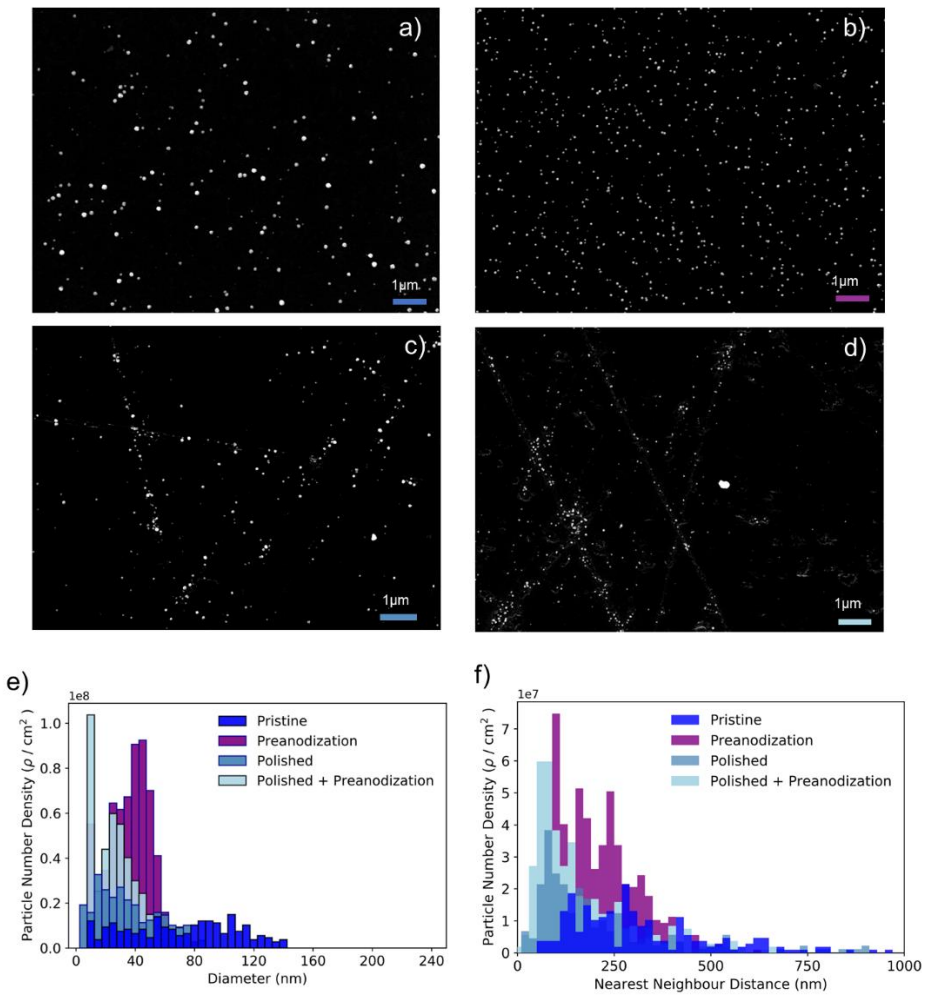

Fig 9. Representative SEM micrographs of copper deposited on the glassy carbon surface under different conditions: a) initial condition (Pristine), b) preanodization, c) polished, and d) polished + preanodization. Histograms of the distribution of diameter (e) and nearest neighbour distance (f) of the copper deposits on the different conditions constructed from the images.

We chose the diameter (D) of the nanoparticles (NPs) formed, NPs density, and the nearest neighbour distance (NND), i.e., the shortest distance between two NPs, as experimental descriptors to assess the effect of the surface state. The formers relate to the amount of deposited material and the latter contains information on how the NPs are distributed over the surface. From SEM images in Fig 9a and 9b, NPs of tens of nanometers and uniformly distributed over the non-polished surfaces can be observed, without following a regular order or array. In contrast, in Fig 9c and 9d, smaller NPs align along the pattern left by the scratches of the mechanical polishing on these surfaces. Interestingly, the formation of the smaller NPs tends to be confined to the defects on these surfaces, whereas outside these defects it is possible to find big NPs on the polished surfaces (see Fig S9 in section S6, SI).

Fig 9e and 9f show the normalized distribution of Ds and NNDs. From the former, we can confirm that polishing tends to form smaller NPs on average, with a narrower distribution in size. Average of 38 (σ=21) nm on the polished surface, and 74 (σ=36) nm on the pristine one. Subjecting the surface to preanodization produces a higher count of smaller NPs, in both cases, with lower dispersion: 39 (σ=14) nm and 30 (σ=18) nm, for the preanodization and polished+preanodization conditions, respectively. A similar effect is disclosed in the NND distributions: as a result of the mechanical scratches, the NPs on the polished surfaces are packed closer together with more counts at lower NND than on the pristine. We also see more counts at lower NND for polished+preanodization than on the preanodization condition. The possibility of producing smaller NPs with preanodization leads to a higher count of NPs in a narrower distribution. Overall, this resulted in a relative high density of NPs under preanodization (6.21 x 10^8 NPs/cm^2), compared to the pristine (2.23 x 10^8 NPs/cm^2). The summary of the physical features is presented in table 2.

Table 2. summary of physical descriptors of the nanostructures deposited under the different conditions

Condition	Average Diameter (±σ)	Average Nearest Neighbour Distance (±σ)	Nanoparticles Density
Pristine	74 (± 36) nm	327 (± 186) nm	2.23 x 10^8 NPs/cm^2
Polished	38 (± 21) nm	228 (± 198) nm	2.73 x 10^8 NPs/cm^2
Preanodization	39 (± 14) nm	206 (± 108) nm	6.21 x 10^8 NPs/cm^2
Polished + Preanodization	30 (± 18) nm	180 (± 141) nm	4.17 x 10^8 NPs/cm^2

To further understand the effect of the pretreatment on the state of the surface, the bare GC surfaces (with no particles deposited) were analyzed by XPS. Fig 10 shows the spectra recorded for every surface pretreatment, which were deconvoluted into five peaks [61,62]. The main peak is located at 284.5 ±1 eV which corresponds to the graphitic carbon (C_g), the peaks centered at 285.0 ±1 eV correspond to C-H, at 286.3 ±1 eV to C-O, at 287.7 ±1 eV to C=O, and at 289.0 ±1 eV to COOH. As detailed in table S2 in section S7 of the Supporting Information, the chemical signature of the carbon substrates changes with every pretreatment. The C-H/C_g ratio of the pristine surface was 0.80, and it increased when subjected to preanodization (1.10) and polishing (0.88) yet decreased under the combination polished+preanodization (0.76). Notably, the amount

of the oxygen-containing groups with respect to the amount of graphitic carbon, C_{ox}/C_g, increased with every pretreatment: from 0.15 on the pristine surface, to 0.24, 0.30, and 0.39 for preanodization, polished+preanodization, and polished, respectively.

The presence of these oxygen-containing groups on the surface (C-O, C=O, COOH) can have a meaningful impact on the electrochemical response. The larger contribution of graphitic structure on the surface can facilitate the oxidation of the GC and the formation of a graphite-oxide layer, leading to a higher number of active sites [63]. These results give further evidence of the modification of the GC surface with the pretreatments and are consistent with the electrochemical measurements presented above. Thus, the C_{ox}/C_g variation follows the same trend as the average OP (table 1), being lowest (less active) for the pristine and highest (more active) on the polished surface.

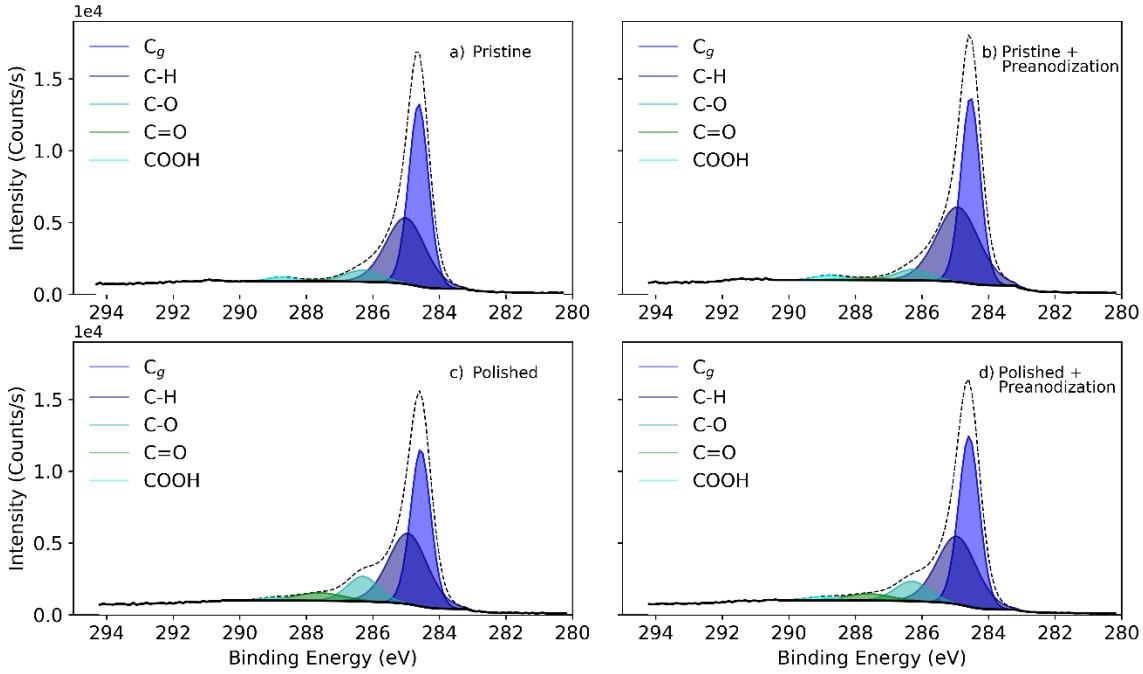

Fig 10. Deconvoluted XPS C1s spectra from the a) pristine, b) preanodization, c) polished and d) polished+preanodization Glassy Carbon bare surface.

DISCUSSION

The nature of active sites: A distribution of activities

The electrochemical activity of an electrode is related in many aspects to the properties of the interface, which triggers the interest to find correlations among the electrochemical features and the surface state (via SEM, TEM, AFM, etc.) [31,39,64–66], and with the nature of the electrolyte [32,67–69]. Yet, the real nature of what compels a surface to be active for nucleation is still elusive, for the most part. The results presented here put in perspective the effect of the different surface pretreatments on the final properties of the deposit and can be discussed in light of our findings of electrochemical activity distributions measured with SECCM.

The overpotential required in the copper electrochemical reduction is a consequence of the work required to form copper nuclei onto the GC, and the crystallographic misfit between the metal adatoms, which favor specific orientations and geometries, and the substrate, consisting of randomly orientated C_g, C-H and C_{ox} atoms. This leads to the notion of an active site for nucleation: the existence of sites/regions on the surface that can contribute differently to the electrochemical reaction is a reasonable assumption considering the variety of structural defects, faceting, edges, cracks, or scratches that can be present intrinsically on a heterogeneous substrate or may be otherwise introduced through a pretreatment. Thus, the glassy carbon should present itself with different features to an incoming reagent owing to the variety of features present at the surface [70]. Hence, a diversity of activities towards an activated process such as EN&G can exist because of local variations in the surface state [25]. Such diversity should exert great influence on the electrode process (as shown here), accounting for preferential sites onto which the nucleation will occur with the highest probability, i.e.*, active sites* where the energy barrier required to form a stable nucleus is smaller.

The classical nucleation theories do not account for the phenomenon of nucleation occurring at different rates at different active sites on the surface and the nature of active sites is not easily identifiable. The dependence on the electrode potential is commonly assumed since many experimental investigations have shown that the number of nuclei does increase with the overpotential applied. The theory of Markov and Kaischew [23] is based on the assumption that the number of active sites is potential-dependent, the active sites are considered as instantly "frozen" with the overpotential applied, with each site being active beyond some value of the electrode potential. Then, one could control the number (or activity) of sites for nucleation on the surface by simply shifting the electrode potential; but the question of the physical/chemical aspect of these sites still remains. For instance, there has been clear evidence that nucleation occurs preferentially on scratches on the electrode surface [59,71,72], as shown here; then altering the physicochemical features can lead to different nuclei densities under the same electrode potential. However, the post-mortem analysis of clusters deposited on macroscopic electrodes does not reflect faithfully the number and location of active sites on the surface, since the development of exclusion zones spreading around nucleated sites leads to deactivation of latent nucleation sites; additionally, the clusters can detach, move or aggregate before being imaged [66,73,74]. Although it is indeed possible to obtain information about the surface state by studying the final stage of the deposit [75], the matter is complicated by said problem. This could also be related to the idea that the active sites are not randomly distributed on the substrate. The theory of Fletcher and Lwin [25]

proposed that the activity is not fixed but rather distributed in a spectrum, which is characteristic of the electrode surface. Kaischew and Mutaftschiew showed that, in the case of mercury nucleation on platinum, the nuclei were preferentially formed onto specific facets, due to the presence of an oxide layer [76]. This idea of oxygen-containing surface features playing the role of active sites has been further supported with experiments of silver and copper nucleation on platinum with a controlled amount of oxygen-containing surface species [77–79]. On the basis of the results presented above, we see a correlation between the presence of the oxygen-containing groups and the electrochemical nucleation activity on the surfaces. We can consider that the introduction of defects on graphitic structures and further oxidation under the different pretreatment are indeed acting as new active sites on the GC surface. It is clear that polishing readily promotes the formation of these C_{ox} groups, especially on the defects introduced on the surface where the nuclei formed preferentially.

With the SECCM we have been able to obtain a new perspective by restricting the area of survey to resolve the individual contribution of different sites on the surface at the microscopic level. This deconvoluted perspective of the electrodeposition process has shown that the nucleation activity on the GC surface is not uniformly distributed, but is rather a continuous non-uniform spectrum, site-dependent, which can be changed by altering the physical and/or chemical properties of the surface itself. The observation of a distribution of activities necessarily follows that there is a distribution of nucleation rates, spread over the electrode surface, as it exhibits different activities on the scale of the experimental probe (diameter ~ 1 µm). The scale itself is a fundamental factor to extract such information: when the EN&G is monitored at the macroscale the whole surface of the electrode is part of the interface at which the reaction occurs, and the nucleation activity that can be extracted this way cannot account for local dispersions, resulting in an averaged-out value. The local dispersions that might be found have been shown to be size-dependent [46,50]. In an energetically-uniform surface, every site would have the same probability of activation, in such cases, it is only relevant to consider their relative locations on the surface. In a non-uniform distribution, however, there will always exist a hierarchy of preferred sites, where the *highly active sites* will have the highest probability to nucleate. Therefore, an active site in this context can be defined as the region of the surface having a local activity greater than its neighbors [80]. In such cases, the distribution of activity introduces another correlation than their relative location, since the influence on the neighbors will depend not only on its location but on its activity as well, having a fundamental impact on the phase formation process (as shown in Fig 9).

The difference in activity then plays an important role in defining which regions can contribute to a greater extent to the overall response. It is clear that polishing creates a more active surface (Fig 8), which leads to early onsets for nucleation. Since the activity distribution is narrow, the different sites will have almost the same probability of activation. When the surface is subjected to preanodization, there is a bigger dispersion in the activity distribution, this allows for multiple nuclei to form and grow at different rates on different sites. The dispersion of the nucleation rates would mitigate the inhibition among nearby clusters and the stationary condition will be attained slower. A narrow distribution could be the result of surveying an overwhelming count of highly active sites that dominate the response early on, as can be seen for the polished surface. Under this condition of non-uniform activity, nucleation will always occur more rapidly on the sites that constitute the lower tail of the distribution, and the dispersion will define how determinant is their contribution to the final response.

We also recognize the possibility that active sites may appear or/and disappear from the surface as a result of independent (electro)chemical processes, concomitant with the EN&G (i.e., oxidation-reduction, surface transformation under potential applied, adsorption/desorption of ions…) as suggested by Milchev [81,82]. Since we have shown that the activity distribution can change after subjecting the surface to prolonged polarization (Fig 8) and that oxygen-containing groups can indeed form on the surface (Fig 10), the hypothesis seems reasonable: these oxygen-containing groups could then disappear from the surface during the cathodic scan, accounting for the disappearance of the active sites thereafter which could explain the shift to higher overpotential between consecutive scans (Fig 3). However, distinguishing between the number of sites and their activity is not trivial; a task that could be tackled by trying to further isolate single sites using pipettes with smaller diameters, approaching the scale of individual nuclei to arrive at traceable and reliable electrochemical descriptors.

Another consideration that can be taken into account with this new local perspective is the variation of the surface tension σ_s. The heterogeneous nucleation process involves the thermodynamic and mechanical equilibrium between three different interfaces: between the (electro)deposited metal phase (m), the electrode surface (e), and solution (s). The equilibrium condition is expressed by the Young equation [1,83]:

$$\sigma_{m,e} + \sigma_{s,m}\cos\theta - \sigma_{s,e} = 0 \qquad \text{Eq 1.}$$

where θ is the contact angle between the electrode surface and the nucleus of the new phase. The barrier for nucleation of the new phase will account for volumetric expansion work and surface expansion work, the latter encompasses the contribution of the different interfaces involved. It is reasonable to expect that $\sigma_{m,e}$, and $\sigma_{s,e}$ have different values at different locations on the electrode surface, which would lead to different energy barriers to overcome. The nucleus contact angle depends on its adhesion energy to the surface, whilst variations in $\sigma_{s,e}$ can originate from differences in the formation of the solution | electrode interface, due to slight differences in how the meniscus “wets” the electrode on each new site. Depending on how sensitive the nucleation energy to the local changes of the surface tensions is, it could lead to wide distributions. Evidence in this direction is the dispersion of currents under diffusion-controlled presented in Fig S10, section S8 of SI: under mass transport limitations the current will be set by the extension of the diffusion fields and geometry of the cell. The dispersion, in this case, could indicate slightly different areas of wetting on different sites. A larger dispersion can be seen on the data surveyed on a pristine surface, compared to the polished one, which could account for the bigger dispersion also seen on the electrochemical activity.

CONCLUSIONS

We have provided an unprecedented perspective of the electrodeposition of Cu on GC, using the SECCM to probe the substrate hundreds of times at the microscale. Leveraging the spatial resolution of the SECCM, we have provided evidence of the existence of a non-uniform distribution of electrochemical activity towards nucleation on GC, supported by SEM and XPS analysis, which can be modified with common surface pretreatments. We have addressed the electrochemical diversity through multiple descriptors and used them to conduct statistical analysis. This work serves as a departure point to conceive new analysis strategies to improve our understanding of the EN&G at the local level and address the real nature of active sites.

The SEM analysis served to establish the impact of the pretreatments on the deposits, particularly showing the NPs aligning along the pattern left by the scratches of the mechanical polishing, as evidence of new highly active sites introduced on the surfaces. This was supported by XPS analysis of the surfaces, showing the presence of oxygen-containing groups in higher proportion after polishing, than on the pristine and preanodization condition, in correlation with the distribution of electrochemical activity disclosed with the SECCM. The introduction of a distribution of activities for EN&G plays an essential role in defining which regions of the electrode largely contribute to the overall macroscopic response, and introduces another correlation, since the influence on their neighbors will depend not only on the relative location of the active sites but on its activity as well.

SECCM has been shown to be a versatile platform to study the diversity of the electrochemical response in the necessary high-throughput fashion and to address the potential and site-dependent diversity with statistical analysis. This novel perspective of the EN&G can help to deconvolute the individual contributions at the local level and reinterpret the conventional response on the basis of a non-uniform activity. Understanding and manipulating the distribution of activity is essential to facilitate the choice or fabrication of appropriate surface conditions to yield a deposit with the desired physical characteristics. Moreover, the non-uniformity of nucleation energies, and therefore nucleation rate dispersion, are concepts that must be taken into account in a satisfactory description of the theory of EN&G.

Electrodeposition, as an extremely sensitive process to the surface, has served to demonstrate the interdependency of the electrochemical evaluation with the local surface state manifesting in many descriptors. The existence of a distribution of electrochemical activity has major implications for several electrode processes of fundamental and applied interests besides electrodeposition, such as electrocatalysis [50,84], electrodissolution [85], gas evolution reactions [33,86], and corrosion [87]. To fully understand and exploit the concept of electrochemical diversity, it becomes extremely relevant to establish correlations between the local electrochemical evaluation and the local features through surface characterization techniques of high spatiotemporal resolution that can be co-located with the same area on the same scale.

ACKNOWLEDGEMENTS

D.T. acknowledges financial support to the Fonds de Recherche dans l'Industrie et dans l'Agriculture (FRIA). The authors are grateful for the support of Lic. Mariana Saavedra in the preparation of the graphical abstract. J.U., M.B. and S. H. acknowledge financial support to the Fonds de la Recherche Scientifique de Belgique (F.R.S.-FNRS) under Grant No. F.4531.19. JU and MB also acknowledge the support from the Fonds Wetenschappelijk Onderzoek in Vlaanderen (FWO, contract G0C3121N). Finally, the authors gratefully acknowledge David Petitjean and Olivier Croquet for technical assistance in setting up the SECCM platform.

REFERENCES

1. B. R. Scharifker and J. Mostany, in *Encyclopedia of Electrochemistry*,, p. 512–540, Wiley, Weinheim, Germany (2003).

2. B. R. Scharifker and J. Mostany, in *Developments in Electrochemistry*, D. Pletcher, T. Zhong-Qun, and D. Williams, Editors, vol. 9781118694, p. 65–75, Jonh Wiley & Sons (2014).

3. J. Ustarroz, T. Altantzis, J. A. Hammons, A. Hubin, S. Bals, and H. Terryn, *Chem. Mater.*, **26**, 2396–2406 (2014).

4. J. Ustarroz, J. A. Hammons, T. Altantzis, A. Hubin, S. Bals, and H. Terryn, *J. Am. Chem. Soc.*, **135**, 11550–11561 (2013).

5. P. Sebastián-Pascual, I. Jordão Pereira, and M. Escudero-Escribano, *Chem. Commun.*, **56**, 13261–13272 (2020).

6. M. Bernal Lopez and J. Ustarroz, *Curr. Opin. Electrochem.*, **27**, 100688 (2021).

7. J. Pu, Z. Shen, C. Zhong, Q. Zhou, J. Liu, J. Zhu, and H. Zhang, *Adv. Mater.*, **32**, 1–28 (2020).

8. D. Kang, T. W. Kim, S. R. Kubota, A. C. Cardiel, H. G. Cha, and K. S. Choi, *Chem. Rev.*, **115**, 12839–12887 (2015).

9. M. E. Hyde and R. G. Compton, *J. Electroanal. Chem.*, **549**, 1–12 (2003).

10. J. Ustarroz, *Curr. Opin. Electrochem.*, **19**, 144–152 (2020).

11. A. Milchev, *Nanoscale*, **8**, 13867–13872 (2016).

12. E. Budevski, G. Staikov, and W. J. Lorenz, *Electrochim. Acta*, **45**, 2559–2574 (2000).

13. A. Bewick, M. Fleischmann, and H. R. Thirsk, *Trans. Faraday Soc.*, **58**, 2200–2216 (1962).

14. G. Gunawardena, G. Hills, I. Montenegro, and B. Scharifker, *J. Electroanal. Chem.*, **138**, 225–239 (1982).

15. E. Budevski, V. Bostanov, and G. Staikov, *Annu. Rev. Mater. Sci.*, **10**, 85–112 (1980).

16. B. R. Scharifker and G. Hills, *Electrochim. Acta*, **28**, 879–889 (1983).

17. B. R. Scharifker and J. Mostany, *J. Electroanal. Chem. Interfacial Electrochem.*, **177**, 13–23

(1984).

18. J. Mostany, J. Mozota, and B. R. Scharifker, *J. Electroanal. Chem.*, **177**, 25–37 (1984).

19. A. Serruya, J. Mostany, and B. R. Scharifker, *J. Chem. Soc. Faraday Trans.*, **89**, 255–261 (1993).

20. W. S. Kruijt, M. Sluyters-Rehbach, J. H. Sluyters, and A. Milchev, *J. Electroanal. Chem.*, **371**, 13–26 (1994).

21. M. E. Hyde, R. M. J. Jacobs, and R. G. Compton, *J. Electroanal. Chem.*, **562**, 61–72 (2004).

22. I. Markov and D. Kashchiev, *J. Cryst. Growth*, **13**–**14**, 131–134 (1972).

23. I. Markov and D. Kashchiev, *J. Cryst. Growth*, **16**, 170–176 (1972).

24. I. Markov, *Thin Solid Films*, **35**, 11–20 (1976).

25. S. Fletcher and T. Lwin, *Electrochim. Acta*, **28**, 237–243 (1983).

26. F. Scholz, *Electrochem. commun.*, **13**, 932–933 (2011).

27. A. Milchev, *J. Electroanal. Chem.*, **457**, 35–46 (1998).

28. A. Milchev, *J. Electroanal. Chem.*, **457**, 47–52 (1998).

29. V. Tsakova, *J. Solid State Electrochem.*, 10–12 (2020).

30. J. V. Zoval, R. M. Stiger, P. R. Biernacki, and R. M. Penner, *J. Phys. Chem.*, **100**, 837–844 (1996).

31. M. Miranda-Hernández, I. González, and N. Batina, *J. Phys. Chem. B*, **105**, 4214–4223 (2001).

32. E. Sosa, G. Carreño, C. Ponce-De-León, M. T. Oropeza, M. Morales, I. González, and N. Batina, *Appl. Surf. Sci.*, **153**, 245–258 (2000).

33. L. Zhang, R. Iwata, L. Zhao, S. Gong, Z. Lu, Z. Xu, Y. Zhong, J. Zhu, S. Cruz, K. L. Wilke, P. Cheng, and E. N. Wang, *Cell Reports Phys. Sci.*, **1**, 100262 (2020).

34. S. A. Hendricks, Y. Kim, and A. J. Bard, *J. Electrochem. Soc.*, **139**, 2818–2824 (1992).

35. J. Velmurugan, J. M. Noël, W. Nogala, and M. V. Mirkin, *Chem. Sci.*, **3**, 3307–3314 (2012).

36. J. Velmurugan, J. M. Noël, and M. V. Mirkin, *Chem. Sci.*, **5**, 189–194 (2014).

37. M. J. Peña, R. Celdran, and R. Duo, *J. Electroanal. Chem.*, **367**, 85–92 (1994).

38. C. L. Bentley, *Electrochem. Sci. Adv.*, 1–18 (2021).

39. I. M. Ornelas, P. R. Unwin, and C. L. Bentley, *Anal. Chem.*, **91**, 14854–14859 (2019).

40. C. L. Bentley, J. Edmondson, G. N. Meloni, D. Perry, V. Shkirskiy, and P. R. Unwin, *Anal. Chem.*, **91**, 84–108 (2019).

41. N. Ebejer, A. G. Güell, S. C. S. Lai, K. McKelvey, M. E. Snowden, and P. R. Unwin, *Annu. Rev. Anal. Chem.*, **6**, 329–351 (2013).

42. M. P. Zach, K. Inazu, K. H. Ng, J. C. Hemminger, and R. M. Penner, *Chem. Mater.*, **14**, 3206–3216 (2002).

43. S. C. S. Lai, R. A. Lazenby, P. M. Kirkman, and P. R. Unwin, *Chem. Sci.*, **6**, 1126–1138 (2015).

44. T. M. Day, P. R. Unwin, and J. V. Macpherson, *Nano Lett.*, **7**, 51–57 (2007).

45. Y. R. Kim, S. C. S. Lai, K. McKelvey, G. Zhang, D. Perry, T. S. Miller, and P. R. Unwin, *J. Phys. Chem. C*, **119**, 17389–17397 (2015).

46. M. Bernal, D. Torres, S. P. Semsari, M. Čeh, K. Žužek Rožman, S. Šturm, and J. Ustarroz, *Electrochim. Acta* (2022).

47. A. Milchev, E. Vassileva, and V. Kertov, *J. Electroanal. Chem. Interfacial Electrochem.*, **107**, 323–336 (1980).

48. S. Fletcher, C. S. Halliday, D. Gates, M. Westcott, T. Lwin, and G. Nelson, *J. Electroanal. Chem. Interfacial Electrochem.*, **159**, 267–285 (1983).

49. T. Le Manh, E. M. Arce-Estrada, M. Romero-Romo, I. Mejía-Caballero, J. Aldana-González, and M. Palomar-Pardavé, *J. Electrochem. Soc.*, **164**, D694–D699 (2017).

50. E. B. Tetteh, L. Banko, O. A. Krysiak, T. Löffler, B. Xiao, S. Varhade, S. Schumacher, A. Savan, C. Andronescu, A. Ludwig, and W. Schuhmann, *Electrochem. Sci. Adv.*, 1–9 (2021).

51. G. Gunawardena, G. Hills, and B. Scharifker, *J. Electroanal. Chem.*, **130**, 99–112 (1981).

52. R. L. Harniman, D. Plana, G. H. Carter, K. A. Bradley, M. J. Miles, and D. J. Fermín, *Nat. Commun.*, **8**, 971 (2017).

53. J. K. Nørskov, J. Rossmeisl, A. Logadottir, L. Lindqvist, J. R. Kitchin, T. Bligaard, and H. Jónsson, *J. Phys. Chem. B*, **108**, 17886–17892 (2004).

54. B. R. Scharifker, J. Mostany, and A. Serruya, *Electrochim. Acta*, **37**, 2503–2510 (1992).

55. G. J. Hills, D. J. Schiffrin, and J. Thompson, *Electrochim. Acta*, **19**, 657–670 (1974).

56. R. C. Engstrom and V. A. Strasser, *Anal. Chem.*, **56**, 136–141 (1984).

57. R. C. Engstrom, *Anal. Chem.*, **54**, 2310–2314 (1982).

58. L. Bodalbhai and A. Brajter-Toth, *Anal. Chim. Acta*, **231**, 191–201 (1990).

59. M. Palomar-Pardavé, M. Miranda-Hernández, I. González, and N. Batina, *Surf. Sci.*, **399**, 80–95 (1998).

60. D. Grujicic and B. Pesic, *Electrochim. Acta*, **50**, 4426–4443 (2005).

61. B. Brunetti, E. De Giglio, D. Cafagna, and E. Desimoni, *Surf. Interface Anal.*, **44**, 491–496 (2012).

62. K. M. Sundberg, W. H. Smyrl, L. Atanasoska, and R. Atanasoski, *J. Electrochem. Soc.*, **136**, 434–439 (1989).

63. A. Dekanski, J. Stevanović, R. Stevanović, B. Ž. Nikolić, and V. M. Jovanović, *Carbon N. Y.*, **39**, 1195–1205 (2001).

64. J. Ustarroz, U. Gupta, A. Hubin, S. Bals, and H. Terryn, *Electrochem. commun.*, **12**, 1706–1709 (2010).

65. J. V. Zoval, J. Lee, S. Gorer, and R. M. Penner, *J. Phys. Chem. B*, **102**, 1166–1175 (1998).

66. H. E. M. Hussein, R. J. Maurer, H. Amari, J. J. P. Peters, L. Meng, R. Beanland, M. E. Newton, and J. V Macpherson, *ACS Nano*, **12**, 7388–7396 (2018).

67. H. E. M. Hussein, H. Amari, B. G. Breeze, R. Beanland, and J. V. Macpherson, *Nanoscale*, **12**, 21757–21769 (2020).

68. E. Plaza-Mayoral, P. Sebastián-Pascual, K. N. Dalby, K. D. Jensen, I. Chorkendorff, H. Falsig, and M. Escudero-Escribano, *Electrochim. Acta*, 139309 (2021).

69. P. Sebastián, L. E. Botello, E. Vallés, E. Gómez, M. Palomar-Pardavé, B. R. Scharifker, and J. Mostany, *J. Electroanal. Chem.*, **793**, 119–125 (2017).

70. J. Cassidy, W. Breen, A. McGee, T. McCormacx, and M. E. G. Lyons, *J. Electroanal. Chem.*, **333**, 313–318 (1992).

71. M. Y. Abyaneh, *Electrochim. Acta*, **27**, 1329–1334 (1982).

72. W. J. Lorenz and G. Staikov, *Surf. Sci.*, **335**, 32–43 (1995).

73. J. Ustarroz, X. Ke, A. Hubin, S. Bals, and H. Terryn, *J. Phys. Chem. C*, **116**, 2322–2329 (2012).

74. M. H. Mamme, C. Köhn, J. Deconinck, and J. Ustarroz, *Nanoscale*, **10**, 7194–7209 (2018).

75. A. Milchev, *Electrochim. Acta*, **28**, 947–953 (1983).

76. R. Kaischew and B. Mutaftschiew, *Electrochim. Acta*, **10**, 643–650 (1965).

77. T. Chierchie and A. Milchev, *Electrochim. Acta*, **35**, 1873–1877 (1990).

78. A. I. Danilov, E. B. Molodkina, and Y. M. Polukarov, *Russ. J. Electrochem.*, **36**, 998–1007 (2000).

79. A. I. Danilov, E. B. Molodkina, A. V. Rudnev, Y. M. Polukarov, and J. M. Feliu, *Electrochim. Acta*, **50**, 5032–5043 (2005).

80. R. L. Deutscher and S. Fletcher, *J. Electroanal. Chem.*, **277**, 1–18 (1990).

81. A. Milchev, *Electrochim. Acta*, **30**, 125–131 (1985).

82. A. Milchev, *Electrochim. Acta*, **31**, 977–980 (1986).

83. D. Branco P., J. Mostany, C. Borrás, and B. R. Scharifker, *J. Solid State Electrochem.*, **13**, 565–571 (2009).

84. P. Ciocci, J.-F. Lemineur, J.-M. Noël, C. Combellas, and F. Kanoufi, *Electrochim. Acta*, **386**, 138498 (2021).

85. L. C. Yule, V. Shkirskiy, J. Aarons, G. West, B. A. Shollock, C. L. Bentley, and P. R. Unwin, *Electrochim. Acta*, **332**, 135267 (2020).

86. T. Zhang, S. Li, Y. Du, T. He, Y. Shen, C. Bai, Y. Huang, and X. Zhou, *J. Phys. Chem. Lett.*, **9**, 5630–5635 (2018).

87. L. C. Yule, C. L. Bentley, G. West, B. A. Shollock, and P. R. Unwin, *Electrochim. Acta*, **298**, 80–88 (2019).